

Research Article

# Photocatalytic degradation of methylene blue dye using synthesized $\text{Co}_x\text{Ni}_{1-x}\text{Fe}_2\text{O}_4$ nanoparticles under direct visible light

\*<sup>1</sup>Seemab Hussnain, <sup>1</sup>Syed Salman Ali, <sup>2</sup>Muhammad Qadeer Alam, <sup>2</sup>Muhammad Hamad Safder, <sup>3</sup>Atia Roman, <sup>3</sup>Tehreem Fatima and <sup>4</sup>Muhammad Asif

<sup>1</sup>Department of Physics, University of Agriculture Faisalabad, Pakistan

<sup>2</sup>Department of Physics, Government College University, Pakistan

<sup>3</sup>Department of Chemistry, National University of Sciences & Technology (NUST), Pakistan

<sup>4</sup>Department of Chemistry, University of Education Lahore, Pakistan

Received 15 Aug 2023, Accepted 10 Sept 2023, Available online 21 Sept 2023, Vol.11, No.3 (Sept 2023)

## Abstract

A cobalt doped nickel ferrites were prepared in this study. Photo catalysts made of cobalt-doped nickel ferromagnetic materials nanoparticles were utilized to degrade dyes. These nanoparticles were synthesized by the co-precipitation technique. A UV-Vis spectrophotometer was used to determine the band gap. These ferrites had band gap between 2.32eV to 2.20eV. The spinel structure of ferrites was characterized X-ray diffraction (XRD) technique. The shape and average size of synthesized nanoparticles was determined by scanning electron microscopy (SEM). Fourier transform infrared FTIR shows metal-oxygen bond in the range of 400-1000 $\text{cm}^{-1}$ . The photocatalytic degradation of dye under UV radiation and direct sunlight was studied. Almost 72 to 92 percent methylene blue dye was degraded in first 100 mints owing to the active octahedral to tetrahedral lattice sites and prevent the recombination of electron/hole pair. The photo-degradation of methylene blue (MB) and a few textile dyes was practised to examine the photocatalytic performance of Co-Ni $\text{Fe}_2\text{O}_4$ . It was observed as the most effective photocatalyst for treating sewage.

**Keywords:** Cobalt chloride hexahydrate; Nickel chloride hexahydrate; Spinel ferrites; Methyl blue dye; Photocatalytic activity; Electron/hole pair recombination mechanism

## 1. Introduction

In recent times, photocatalytic oxidation (PCO) of dyes employing ferrites has attracted enormous interest. Wastewater contains highly hazardous dyes that are toxic to humans and many living organisms, as well as having serious effects on an environment like soil, air, animals, water, and plants. Dyes are huge pollutants in several industries, like textile, plastic, paper, cosmetics, leather, etc., in which they are employed for coloring purposes [1-6]. The excessive release of waste harmful dyes, including rhodamine b, methylene blue, and methylene orange, into water ponds and soils threatens environmental protection. Around 0.7 million tonnes of organic dyes are produced per year, and during the process of dying, 12% of the whole is directly discharged into the ecosystem [7, 8]. Dye contamination in wastewater has been associated with serious diseases, including cancer, heart disease, DNA damage, and sclerosis [9]. Nano-spinel ferrites ( $\text{AB}_2\text{O}_4$ ) have previously been reported as the most promising photo-catalysts due to their high stability, narrow band gap, low cost, superior adsorption potential, easy regenerability, environmentally friendly nature, and stability, which make them appropriate applications for photocatalytic performance.

Their comparatively small band gap of 2.0 eV is another factor supporting their viability [10]. Several transition metal oxides, such as  $\text{Ag}_2\text{O}$  [11],  $\text{TiO}_2$  [12],  $\text{MoS}_2$ ,  $\text{CdS}$  [13],  $\text{ZrO}_2$  [14],  $\text{ZnS}$  [15],  $\text{ZnO}$  [16],  $\text{NiO}$  [17],  $\text{Cu}_2\text{O}$  [18], and  $\text{Fe}_2\text{O}_3$  [19], have been researched in the past for photocatalytic dye degradation. Among these, nickel ferrites ( $\text{NiFe}_2\text{O}_4$ ) have received the most attention because of their narrow band gap of 2.2 eV, low cost, environmentally friendly behavior, reduce eddy current losses, magnetic properties, high chemical and thermal stability, and high resistivity [20]. Furthermore, the photocatalytic behavior of photo-catalysts based on nickel ferrites can be enhanced even further by adjusting their band gap or by substituting with other transitional/rare earth metals [21]. Nickel ferrite has the inverse spinel framework, wherein a ferric ( $\text{Fe}^{3+}$ ) ion is equally distributed among the tetrahedral and octahedral lattice points in this class of structures, while nickel ( $\text{Ni}^{2+}$ ) ion is distributed only in octahedral sites.  $\text{NiFe}_2\text{O}_4$  is a popular soft magnetic nanomaterial that has a low saturation magnetization and coercivity value [22, 23]. The advantages of cobalt ferrite over other ferrites are its soft magnetic nature, good chemical stability, superior electromagnetic efficiency,

\*Corresponding author's ORCID ID: 0009-0000-2799-682X

DOI: <https://doi.org/10.14741/ijaie/v.11.3.1>

and hardness [24-28]. Cobalt is among several dopants ( $Zn^{2+}$ ,  $Cu^{2+}$ ,  $Co^{2+}$ , etc.) that prefer to fill octahedral sites as well as redistribute cations across two sites.

However, cobalt is a type of hard magnetic material; nickel ferrite substituted with cobalt displays a large intrinsic coercivity and strong magnetocrystalline anisotropy constants [29-31]. The combination of the soft and hard natures of both the ferrites leads to improved magnetic characteristics, which enable Co-doped Ni ferrite ( $Co_xNi_{1-x}Fe_2O_4$ ) nanocrystals appropriate for improving photocatalytic degradation. Thus, cobalt doping enhances the photocatalytic behavior. The materials employed as photocatalysts involve metal oxide and metal sulfide, as well as magnetic semiconductors, quantum dots, and quantum dot/semiconductor oxide composites [32-36].

Still, a few publications have described the photodegradation of the dyes using ferrites as catalysts [37-40]. Kakhki et al. (2017) synthesized the cobalt doped nickel ferrite nanocomposite. The photocatalytic performance of  $Co_xNi_{1-x}Fe_2O_4$  was examined using the photodegradation of methyl blue and several industrial organic dyes under direct visible light. These ferrites were found to be superior photocatalysts in the dye degradation, with a  $0.01 \text{ min}^{-1}$  reaction rate for methyl blue [37]. Cai-Yun et al. (2020) described the simple preparation of  $CoFe_2O_4$  and its uses in the decomposition of organic dyes like methyl blue and rhodamine B. They noted that  $CoFe_2O_4$  was an efficient photocatalyst in dye degradation, with  $0.213 \text{ min}^{-1}$  and  $0.198 \text{ min}^{-1}$  reaction rates for RhB and MB, respectively [38]. Jadhav et al. (2021) studied the photocatalytic performance of  $NiFe_2O_4$  using the methyl blue dye degradation as the model compound. The results revealed that the produced nanoparticles had strong photocatalytic performance against dye decomposition. After 60 minutes under a direct visible light, the degradation reaches 98.23% in an addition of nickel ferrite nanoparticles [39]. Chahar et al. (2021) synthesized the cobalt-doped zinc ferrite ( $Co_xZn_{1-x}Fe_2O_4$ ) nanoparticles with a composition of  $x = 0.0, 0.1, 0.2, 0.3, 0.4,$  and  $0.5$ . It was noted that the methyl blue degradation improved with the increase in Co concentration. Under direct visible light, the degradation performance reached 77% for  $x = 0.5$  and was as low as 65% for  $x = 0.0$  after 1 hour. As a result,  $Co_xZn_{1-x}Fe_2O_4$  ferrite is a viable material for water purification [40]. Various different methods have been employed to prepare these kinds of ferrites in order to obtain nanoparticles with the appropriate structure and shape. Co-precipitation, hydrothermal, sol-gel, and solvothermal procedures are among the most widely used chemical processes due to their low cost, ability to create particles that have a specific shape and size, and high chemical homogeneity [36, 41-43]. Choosing the appropriate approach is believed to be the key to obtaining high-quality ferrite nanoparticles. However, the co-precipitation technique is widely used due to its reproducibility and ease, but it mostly results in the

precipitation of relatively broad-shaped nanocrystals. In this study, Ni ferrites ( $NiFe_2O_4$ ) and Co-doped Ni ferrites (i.e.,  $Co_xNi_{1-x}Fe_2O_4$ ;  $x = 0.0, 0.15, 0.30,$  and  $0.45$ ) nanoparticles were prepared using the chemical co-precipitation method, and their characteristics were characterized before evaluating their uses as the photocatalysts in the degradation of MB dye. The photocatalytic, morphological, optical and structural properties were examined by X-ray Diffraction (XRD), scanning electron microscopy (SEM), and Fourier transform infrared spectroscopy (FT-IR), and UV-visible (UV-Vis) spectroscopy. The findings of this work may facilitate the ability to use Co-doped Ni ferrite nanoparticles in photocatalysis.

## 2. Experimental

### 2.1 Materials

Nickel chloride hexahydrate ( $NiCl_2 \cdot 6H_2O$ , 99%), cobalt chloride hexahydrate ( $CoCl_2 \cdot 6H_2O$ , 99%), ferric chloride hexahydrate ( $Fe_2Cl_3 \cdot 6H_2O$ , 99%) from SIGMA-ALDRICH, sodium hydroxide (NaOH, 98%) from DAEJUNG, and Polyethylene glycol [ $H(CH_2CH_2O)nOH$ ], from DAEJUNG. All the materials were used without additional purification.

### 2.2 Preparation of Ni-Co ferrites

The nickel ferrite (NF) and cobalt-doped nickel ferrite (CNF) nanoparticles with the substitution  $Ni_{1-x}Co_xFe_2O_4$  ( $x = 0.0, 0.15, 0.30,$  and  $0.45$ ) were prepared by a simple co-precipitation approach. A stoichiometric amount of Ferric chloride hexahydrate, nickel chloride hexahydrate, and cobalt chloride hexahydrate was dissolved into 100 mL of distilled water using the magnetic stirrer. The NaOH (9 g) solution was used as a precipitation reagent. Before adding the NaOH dropwise, 0.05 g of PEG-4000 as a surfactant was added to a salt solution under continuous stirring. When the resulting solution reached  $90 \text{ }^\circ\text{C}$ , a solution of NaOH was carefully added dropwise to maintain the solution's pH at about 13. After that, the precipitates were washed with distilled water several times until the pH reached 7. The resultant precipitates were first dried at  $180 \text{ }^\circ\text{C}$  in an oven overnight to eliminate the water content. The dark brown precipitates were ground using the pestle and mortar to convert them into powder. The obtained samples were calcined to  $600 \text{ }^\circ\text{C}$  in a furnace for 6 hours to produce the spinel ferrites phase. The produced samples were carefully characterised using cutting-edge tools.

### 2.3 Characterization techniques

The XRD analysis carried out using a Bruker D2 Phaser X-ray diffractometer with  $Cu-K\alpha$  radiation ( $\lambda = 0.15406 \text{ nm}$ ) exhibited the crystalline nature of the prepared nanomaterials. The SEM (Nova Nano) was used for examining the morphology of the produced CNF nanomaterials. Fourier transform infrared (FT-IR)

spectroscopy was used to identify the functional groups of CNF nanomaterials with a FT-IR spectrophotometer (Cary-630). The optical properties of synthesised CNF nanomaterials and amount of methylene blue (MB) during degradation were examined using a T80 UV-Vis spectrometer.

#### 2.4 Photocatalytic activity

The photocatalytic behavior of the synthesized cobalt-doped nickel ferrite (CNF) samples was evaluated by degrading methylene blue (MB) dye in an aqueous solution upon direct sunlight irradiation. Specifically, 50 mg of CNF particles were added to 50 mL of a 10 mg/L MB solution. The mixture was continuously stirred in the dark for 30 minutes to allow equilibrium to be reached between the dye solution and catalyst through adsorption and desorption processes. Following the addition of 2 mL of 30% hydrogen peroxide ( $H_2O_2$ ), the solution was exposed to illumination while continuing to stir. Aliquots of 3 mL were extracted periodically and centrifuged to separate out the CNF particles. The amount of MB remaining in the aqueous solution after each time interval was analyzed using a UV-Vis spectrophotometer, which measures the maximum absorption of light by MB at its characteristic wavelength. This allowed quantification of the degree of MB degradation over time under the combined photocatalytic effects of the CNF and  $H_2O_2$  when subjected to visible light irradiation. Kinetic studies were carried out by monitoring the reduction in MB concentration as a function of illumination time to evaluate the photocatalytic performance of the synthesized CNF samples for removal of organic dyes from water.

### 3. Results and discussion

#### 3.1 XRD

X-ray diffraction (XRD) was used to characterize the synthesized nanoparticles. XRD provides information about crystal structure by detecting scattered X-ray intensities at specific angles related to a material's lattice spacings. Diffracted peaks in the XRD patterns correspond to different crystal planes of the material. Analysis of nickel ferrite and cobalt-doped nickel ferrite samples via XRD confirmed the formation of crystalline cubic spinel ferrite nanoparticles. Peak positions and intensities indicated phase composition and crystallinity. Characteristics like average crystallite size, lattice constant, and volume were obtained from the XRD patterns and helped analyze structural changes with varying cobalt concentration.

Phase testing using the XRD technique has been conducted to confirm the formation of crystalline cubic spinel ferrite nanoparticles. The XRD patterns of nickel ferrites (NF) and cobalt-doped nickel ferrite (CNF) have been shown in Figs. 1 and 2, respectively, with the concentrations of  $x = 0.00, 0.15, 0.30,$  and  $0.45$ . The

phase purity and crystallinity with space group  $Fd\bar{3}m$  of  $NiFe_2O_4$  nanoparticles have been observed by diffraction pattern, as shown in Fig. 1. The sample contains impurities that may be attributed to other nickel and iron oxides ( $\alpha-Fe_2O_3$ ) [44]. The peaks are observed at the  $2\theta$  values of  $30.45^\circ, 35.8^\circ, 43.56^\circ, 54.19^\circ,$  and  $57.92^\circ$ , which correspond to crystalline planes of (220), (311), (400), (422), and (511), respectively. The average crystallite size, lattice constant, volume, lattice strain, micro strain, dislocation density, and X-ray density have been found to be 18 nm, 8.29 Å, 570.9 Å<sup>3</sup>,  $5.3 \times 10^{-3}$ ,  $1.94 \times 10^{-3}$  (lines<sup>-2</sup>/m<sup>-4</sup>),  $3.19 \times 10^{15}$  (lines/m<sup>2</sup>), and 5.53 (gm/cm<sup>3</sup>), respectively, and shown in Table 1. The main sharp peak (311) confirmed that the NFNPs have an ultra-fine crystalline cubic spinel structure. The fine reflection Miller indices were observed for all samples in Fig. 2, whereas for the compositions of 0.00, 0.15, and 0.30, the additional phases were seen. This is because of the small quantity of cobalt (Co) content.

However, because of the preparation conditions at the time of formation, these samples contain second phases. Impurity peaks of  $\alpha-Fe_2O_3$  have been marked by a small star (\*), as shown in Fig. 2. Besides that, the XRD pattern of CNF for  $x = 0.45$  shows the high purity and crystallinity of the sample because there are no additional peaks appear, indicating the intensive peak of 311 at  $35.94^\circ$ . Therefore, the ( $Co_{0.45}Ni_{0.55}Fe_2O_4$ ) material demonstrates the single-phase cubic spinel structure. The NF and CNF materials have same crystal planes which indicate that the concentration of  $Co^{2+}$  ions occupy interstitial space in the cubic spinel structure of  $Co_xNi_{1-x}Fe_2O_4$  with no significant phase change [45]. The slight shift in crystalline peaks of ( $Co_{0.15}Ni_{0.85}Fe_2O_4$ ), ( $Co_{0.30}Ni_{0.70}Fe_2O_4$ ), and ( $Co_{0.45}Ni_{0.55}Fe_2O_4$ ) in Fig. 3 shows lattice volume expansion because  $Co^{2+}$  has a greater radius (0.74Å) than  $Ni^{2+}$  radii (0.63Å). The crystalline peaks shifting towards the lower side of the spectrum with the different concentrations of cobalt exhibit the transformation of iron ( $Fe^{+3}$ ) ions from a tetrahedral site to an octahedral site [46]. The average particle size, lattice constant, micro strain, lattice strain, dislocation density, X-ray density, and volume for CNF are calculated, and mentioned in Table 1. From values it is verified that volume and lattice constant increase with increasing the concentration of Co because the  $Co^{2+}$  (0.74 Å) with larger atomic radii substitutes the  $Ni^{2+}$  (0.69 Å) with smaller atomic radii on the octahedral sites. As the X-ray density and lattice constant are inversely related to each other, its value drops (5.61–5.57 gm/cm<sup>3</sup>) as the lattice constant increases (8.25–8.27 Å). Since the lattice constant may be directly related to volume, the volume of the unit cell increases from 562 to 566 Å<sup>3</sup> [45]. The change in particle sizes with Co concentration is not regular because of the interior micro stain during a reaction [46]. The highest peak at 311 indicates a slight shift of  $0.06^\circ$  in lower range of  $2\theta$  for CNF,  $x = 0.45$  w.r.t CNF,  $x$

=0.15 as shown in Fig. 4. Moreover, this effect is minor, confirming that cobalt and nickel occupy similar sites.

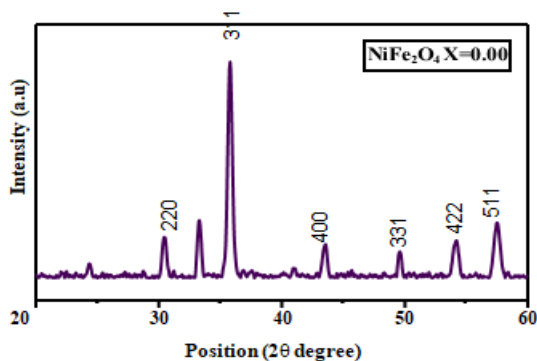


Fig. 1 XRD pattern of NiFe<sub>2</sub>O<sub>4</sub>

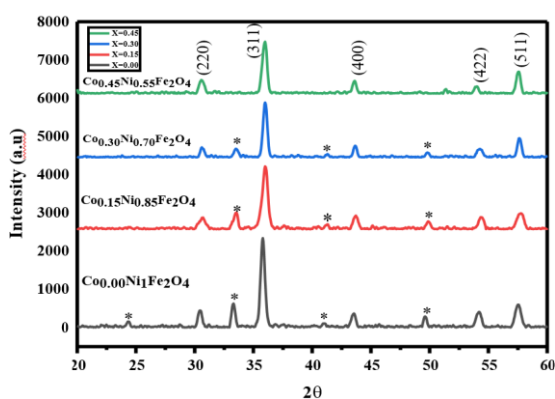


Fig. 2 XRD patterns of Co doped NiFe<sub>2</sub>O<sub>4</sub>

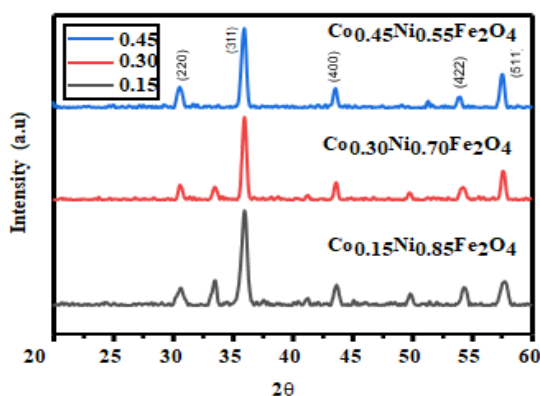


Fig. 3 XRD patterns indicate a slight shift towards lower angle

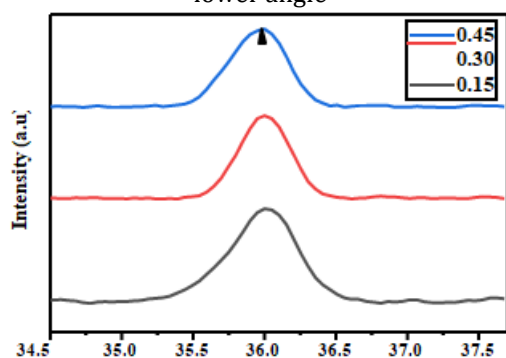


Fig. 4 A close view of highest sharp peak (311) of CNF samples

**Table 1** Structural parameters of synthesized Co<sub>x</sub>Ni<sub>1-x</sub>Fe<sub>2</sub>O<sub>4</sub> with different contents of cobalt (x = 0.00, 0.15, 0.30, 0.45)

Structural Parameters	X=0.0 0	X=0.1 5	X=0.30	X=0.45
2θ Value for Highest Sharp (311) Peak	35.8	36.01	35.95	35.94
d-spacing for (311) Peak	2.50	2.49	2.49	2.49
Average crystallite Size D (nm)	18.00	15.04	20.01	19.12
Average Lattice Constant a (Å)	8.29	8.25	8.26	8.27
Average X-ray Density (gm/cm <sup>3</sup> )	5.532	5.61	5.58	5.57
Average Volume a <sup>3</sup> (Å <sup>3</sup> )	570.9	562.7	565.2	566.8
Average Dislocation Density × 10 <sup>15</sup> (lines/m <sup>2</sup> )	0.003	0.004	0.0026	0.0029
Average Lattice Strain × 10 <sup>-3</sup>	5.345	6.544	4.9006	5.3291
Average Micro Strain × 10 <sup>-3</sup> (lines <sup>-2</sup> /m <sup>-4</sup> )	1.945	2.336	1.7650	1.8480

The acquired FTIR spectra are shown in Fig. 5. The bands are caused by the vibrational functional groups found in the starting compounds and are clearly visible in the spectra of as-calcined materials. They mostly appear in the range of 4000 cm<sup>-1</sup>–1000 cm<sup>-1</sup>. The peaks observed at 1045 cm<sup>-1</sup>, 1646 cm<sup>-1</sup>, 2342 cm<sup>-1</sup>, and 3400 cm<sup>-1</sup> are assigned to the distinctive bands of NO<sub>3</sub><sup>-</sup> (carboxyl groups), stretching of C-H bands, and hydrogen-bonded O-H group, respectively [37, 47, 48].

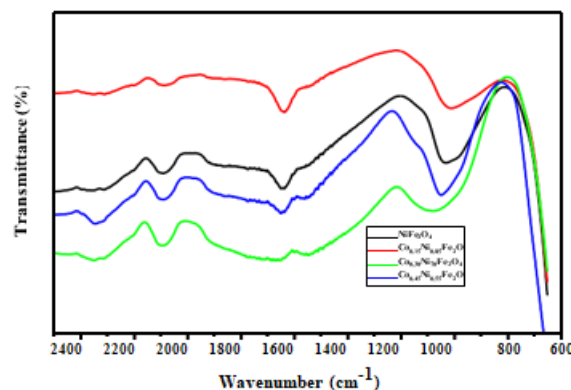


Fig. 5 FTIR spectrums of NF and Co-doped NiFe<sub>2</sub>O<sub>4</sub>

All of the carboxyl, hydroxyl, or nitrate groups occur with lower intensity because of the high temperature created during combustion. The band position observed at higher wavenumber  $\nu_1$  (558 cm<sup>-1</sup>–600 cm<sup>-1</sup>) is attributed to the intrinsic stretching vibrations of metal at a tetrahedral site as Mtetra ↔ O. The band position at lower wavenumber  $\nu_2$  (440 cm<sup>-1</sup>–445 cm<sup>-1</sup>) is attributed to metal stretching at the octahedral site M octa ↔ O. Whereas  $\nu_2$  and  $\nu_1$  could not be observed due to instrumentation restrictions. It is intriguing to observe that the characteristic band position  $\nu_1$  exhibits a change towards the low-frequency side

when the contents of cobalt substitution increase. Such a resemblance is observed because of the slight difference between the atomic weights of cobalt ( $58.9332\mu$ ) and nickel ( $58.6934\mu$ ) [49].

### 3.2 UV-Vis spectroscopy

$\text{NiFe}_2\text{O}_4$  and Co-doped Ni ferrites demonstrate visible light absorption, as seen in Fig. 6. Therefore, it may be inferred that these nanoparticles might exhibit photocatalytic activity when exposed to visible light. From Figs. 6 (a and b), it is evident that  $\text{Co}_{0.45}\text{Ni}_{0.55}\text{Fe}_2\text{O}_4$  has a larger absorbance range (227 nm) in the visible light spectrum than  $\text{NiFe}_2\text{O}_4$  (240 nm), and as a result, they have higher photocatalytic activity. The creation of extra energy levels nearby the valence band, increasing inhomogeneity, localized state density, and varying crystallite sizes of materials can be responsible for the bandgap energies decreasing as the content of Co doping increases [50]. Hence,  $\text{Co}_{0.45}\text{Ni}_{0.55}\text{Fe}_2\text{O}_4$  (2.20 eV) acts as a useful visible light-driven photocatalyst due to the decreased band gap compared to NF (2.32 eV) materials, as shown in Figs. 4 (c and d).

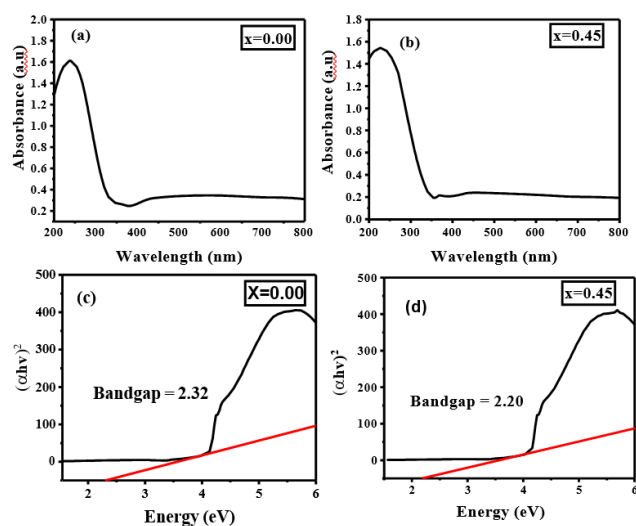


**Fig. 6** Uv-Vis spectra of a) NF and b) CNF ( $x=0.45$ ), Tauc's plot acquired for c) NF and d) CNF ( $x=0.45$ )

### 3.3 SEM

SEM is used to examine the particle size and morphology of nanoparticles. In Figs. 7 (a–b) and 8 (a–b), the occurrence of nanoparticles can be observed in both NF and NCF materials. The spherical-shaped particles are shown in the SEM images of  $\text{NiFe}_2\text{O}_4$  and Co ( $x = 0.45$ )-doped  $\text{NiFe}_2\text{O}_4$  nanosized particles. The average particle sizes of NF and CNF ( $x = 0.45$ ) are  $83.74 \pm 22.87$  nm and  $26.5 \pm 17.65$  nm, respectively, as argued from statistically significant histograms (Figs. 7c and 8c). The fact that the particle size is greater than the crystallite size suggests that grains are made up of many crystals. Hence, it shows that doping with Co causes an increase in average particle size.

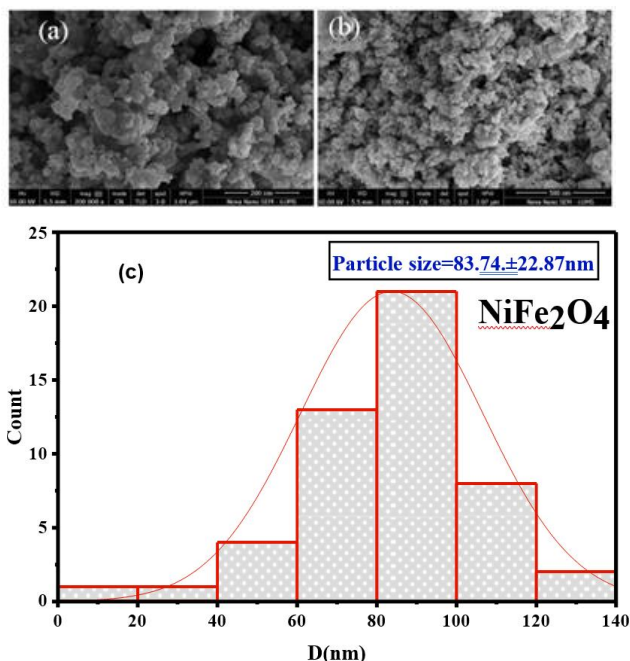


**Fig. 7** (a, b) SEM images of  $\text{NiFe}_2\text{O}_4$ , (c) Statistical histogram of size distribution of  $\text{NiFe}_2\text{O}_4$

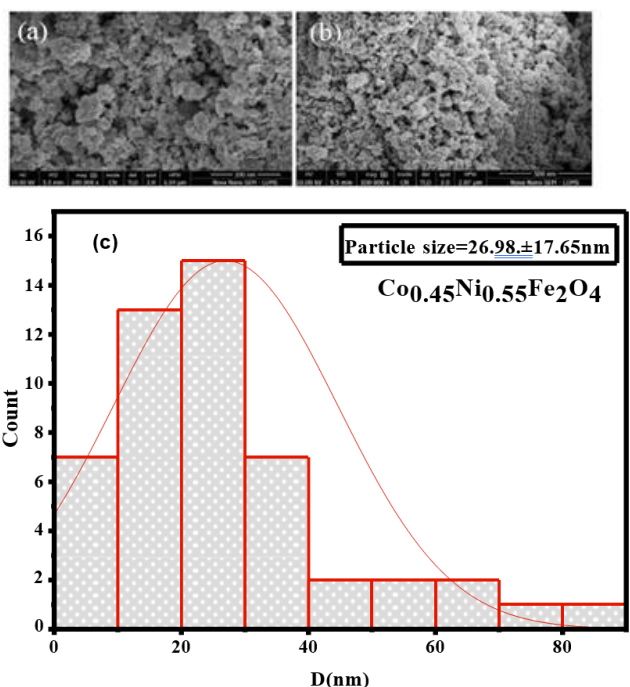


**Fig. 8** (a, b) SEM images of CNF ( $x=0.45$ ), (c) Statistical histogram of size distribution of CNF ( $x=0.45$ )

### 3.4 photocatalytic studies

$\text{Co}_x\text{Ni}_{1-x}\text{Fe}_2\text{O}_4$  ( $x = 0.0, 0.15, 0.30, \text{ and } 0.45$ )

nanoparticles were studied in order to investigate the impact of visible light on MB dye degradation. The following equation was used to determine the percentage of photocatalytic degradation:

$$\text{Degradation percentage} = A_0 - A_t / A_0 \times 100(\%) \quad (1)$$

Here  $A_0$  is the initial absorption of the MB mixture, and  $A_t$  represents the absorption at various ultraviolet (UV) radiation durations. As demonstrated in Fig. 9, when Co is doped into  $\text{NiFe}_2\text{O}_4$  nanoparticles ( $x = 0.45$ ), the degradation behaviour increases to 92% in 100 minutes from 72% with NF ( $x = 0.00$ ). Therefore, the concentration with the greatest ( $x = 0.45$ ) Co content is selected as the best for further studies.

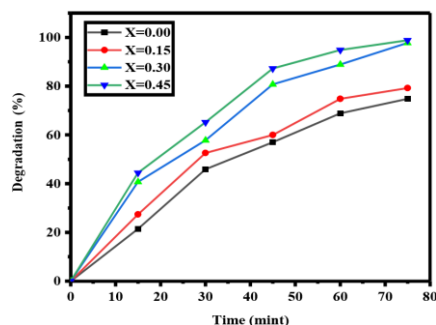


Fig. 9 Degradation percentage of MB

The most significant factors that describe photocatalytic behaviour are photocatalytic characteristics, which are dependent on the particle size, surface area, and quantity of dopant substances. Thus, we explored the photocatalytic efficiency of methylene blue (MB) under direct sunlight by comparing pure nickel and Ni-substituted cobalt ferrites. Four comparative spectrums for MB dye degradation with  $\text{Co}_x\text{Ni}_{1-x}\text{Fe}_2\text{O}_4$  ( $x = 0.0, 0.15, 0.30,$  and  $0.45$ ) nanoparticles are exhibited below in Fig. 10. The UV visible spectra of MB dye for different concentrations of  $\text{Co}^{2+}$  ions in nickel spinel ferrite lattice with peaks at 660 nm confirming the presence of methylene blue. Fig. 10 represents the graphs of NF and CNF nanoparticles at different time intervals and pH conditions, indicating the loss of absorbance ability of the dye with time. The decolorization efficiency is calculated from the intensity of absorption spectra at different time intervals. This obtained result demonstrates that as-prepared  $\text{Co}_{0.45}\text{Ni}_{0.55}\text{Fe}_2\text{O}_4$  nanoparticles have a high potential to be applied as a favorable and appropriate material for photocatalytic applications under the illumination of sunlight.

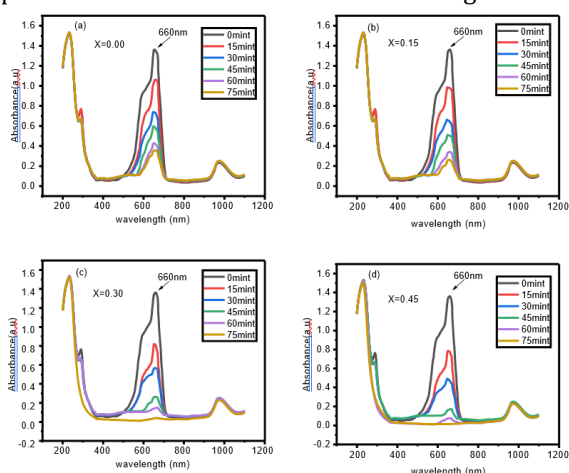


Fig. 10 MB degradation spectrums of a) pure NF b) CNF  $x=0.15$ , c) CNF  $x=0.30$ , and d) CNF  $x=0.45$

### 3.5 Kinetic test for MB dye degradation

The photocatalytic behavior of NF and  $\text{Co-NiFe}_2\text{O}_4$  nanomaterials was occurred by analyzing the kinetic tests of aqueous MB dye degradation solutions under direct sunlight (visible) light [8, 36].

$$\ln(A_0/A_t) = kt \quad (2)$$

Where  $A_0$  and  $A_t$  are the primal concentrations of the dye at a specific irradiation period and  $k$  is the pseudo-first order rate constant. For each experiment, the rate constant ( $k$ ) of all the dye derivatives was calculated using the plot of  $\ln A/A_0$  versus the time. From Fig. 11, the rate constant of  $\text{Co}_{0.45}\text{Ni}_{0.55}\text{Fe}_2\text{O}_4$  shows higher activity ( $0.013 \text{ min}^{-1}$ ) compared to  $\text{NiFe}_2\text{O}_4$  ( $0.023 \text{ min}^{-1}$ ) under direct visible light.

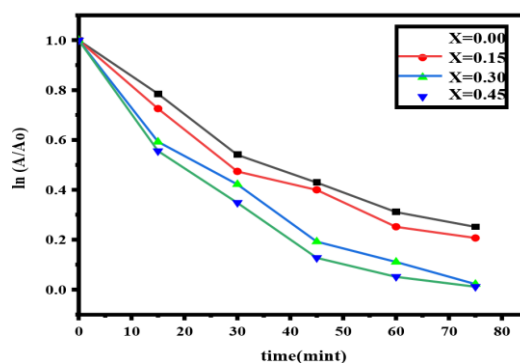


Fig. 11  $\ln A/A_0$  versus time plot graph to find the rate constant

### 3.6 Possible photocatalytic system

There are various techniques used for the degradation of dyes, such as photocatalysis, filtration, reverse osmosis, and adsorption, but photocatalysis is preferable to adsorption since photocatalysts oxidizes/degrades dyes by the hydroxyl radical action after the absorption of sunlight. We have hypothesized a potential explanation for the improved photocatalytic capacity of the degradation MB in the Co-Ni ferrite framework based on the findings of the experiments. Although NF may be driven by visible light, it has a greater rate of photoinduced electron-hole pair recombination than CNF particles, which results in a smaller amount of luminescence for the degradation of MB when exposed to visible light.

On the other hand, due to the NCF system's narrow band gap, more electrons may be stimulated from the valence band (VB) to conduction band (CB) while at the same time, the same number of holes are created in the VB. Therefore, the MB molecules can be immediately converted into  $\text{CO}_2$  and  $\text{H}_2\text{O}$  by holes. While, the  $\text{O}_2$  can be further reduced to produce more OH, which may also mineralize MB molecules into  $\text{H}_2\text{O}$  and  $\text{CO}_2$ . It can be inferred that under direct visible light,  $h^+$  and OH were the primary active constituents of CNF photocatalysts in aqueous MB

solution. The photocatalytic mechanism may be explained in Fig. 12 based on the aforementioned analysis.

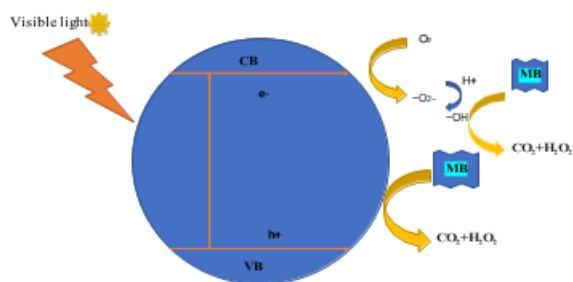


**Fig. 12** Designed mechanism for MB dye degradation by the CNF nanoparticles

## Conclusions

Nanosized cobalt doped nickel ferrite nanoparticles ( $\text{Ni}_{1-x}\text{Co}_x\text{Fe}_2\text{O}_4$ ) with ( $x = 0.0, 0.15, 0.30, \text{ and } 0.45$ ) were prepared with a facile chemical coprecipitation method. The synthesized materials were characterized by different analytical techniques, for instance, XRD, FTIR, UV-Vis, and SEM. The nanomaterials showed photo-degradation of MB under direct sunlight. The findings represent Co- ( $x=0.45$ )  $\text{NiFe}_2\text{O}_4$  has greater photocatalytic effect than nickel ferrite. MB was about 72% degraded in NF photocatalyst, whereas 92% degradation was shown in the case of  $\text{Co}_{0.45}\text{Ni}_{0.55}\text{Fe}_2\text{O}_4$  material after irradiation for 100 minutes in the direct sunlight. Consequently, CNF nanoparticles was used in heterogeneous photocatalysis to absorb photons from the incoming radiation, and oxidation/reduction reactions then efficiently degrade pollutants.

## References

- [1] Liu, S.-Q., et al., Magnetic nickel ferrite as a heterogeneous photo-Fenton catalyst for the degradation of rhodamine B in the presence of oxalic acid. *Chemical Engineering Journal*, 2012. 203: p. 432-439
- [2] Jia, Z., et al., A new strategy for the preparation of porous zinc ferrite nanorods with subsequently light-driven photocatalytic activity. *Materials Letters*, 2011. 65(19-20): p. 3116-3119.
- [3] Jadhav, S., et al., Effect of sintering on photocatalytic degradation of methyl orange using zinc ferrite. *Materials letters*, 2011. 65(2): p. 371-373
- [4] Li, X., et al., A general, one-step and template-free synthesis of sphere-like zinc ferrite nanostructures with enhanced photocatalytic activity for dye degradation. *Journal of colloid and interface science*, 2011. 358(1): p. 102-108.
- [5] Su, M., et al., Mesoporous zinc ferrite: synthesis, characterization, and photocatalytic activity with  $\text{H}_2\text{O}_2$ /visible light. *Journal of hazardous materials*, 2012. 211: p. 95-103.
- [6] Wang, X., et al., Enhanced visible-light-response photocatalytic activity of bismuth ferrite nanoparticles. *Journal of alloys and compounds*, 2011. 509(23): p. 6585- 6588.
- [7] Carmen, Z. and S. Daniela, Textile organic dyes-characteristics, polluting effects and separation/elimination procedures from industrial effluents-a critical overview. Vol.2012: IntechOpen Rijeka.
- [8] Sharma, R. and S. Singhal, Structural, magnetic and electrical properties of zinc doped nickel ferrite and their application in photo catalytic degradation of methylene blue. *Physica B: Condensed Matter*, 2013. 414: p. 83-90.
- [9] Khan, M.A. and A.M. Ghouri, Environmental pollution: its effects on life and its remedies. *Researcher World: Journal of Arts, Science & Commerce*, 2011. 2(2): p. 276-285.
- [10] Dhiman, P., et al., Nanostructured magnetic inverse spinel Ni-Zn ferrite as environmental friendly visible light driven photo-degradation of levofloxacin. *Chemical Engineering Research and Design*, 2021. 175: p. 85-101.
- [11] Ullah, S., et al., Enhanced photoactivity of  $\text{BiVO}_4/\text{Ag}/\text{Ag}_2\text{O}$  Z-scheme photocatalyst for efficient environmental remediation under natural sunlight and low- cost LED illumination. *Colloids and Surfaces A: Physicochemical and Engineering Aspects*, 2020. 600: p. 124946
- [12] Noda, C., et al., Synthesis of three-component  $\text{C}_3\text{N}_4/\text{rGO}/\text{C-TiO}_2$  photocatalyst with enhanced visible-light responsive photocatalytic de $\text{NO}_x$  activity. *Chemical Engineering Journal*, 2020. 390: p. 124616.
- [13] Shenoy, S., K. Tarafder, and K. Sridharan, Graphitic  $\text{C}_3\text{N}_4/\text{CdS}$  composite photocatalyst: Synthesis, characterization and photodegradation of methylene blue under visible light. *Physica B: Condensed Matter*, 2020. 595: p. 412367.
- [14] Reddy, C.V., et al., Ni-dopant concentration effect of  $\text{ZrO}_2$  photocatalyst on photoelectrochemical water splitting and efficient removal of toxic organic pollutants. *Separation and Purification Technology*, 2020. 252: p. 117352.
- [15] Yan, S., et al., One-step synthesis of  $\text{ZnS}/\text{BiOBr}$  photocatalyst to enhance photodegradation of tetracycline under full spectral irradiation. *Materials Letters*, 2020. 276: p. 128232.
- [16] Chang, C.-J., et al., Improved  $\text{H}_2$  production of  $\text{ZnO}@ \text{ZnS}$  nanorod-decorated Ni foam immobilized photocatalysts. *International Journal of Hydrogen Energy*, 2021. 46(20): p. 11357-11368.
- [17] Mohamed, R. and F.A. Harraz, Photoreduction coupling of  $\text{NiO}/\text{SiO}_2$  nanocomposite with palladium and yttria nanoparticles: Visible-light-driven photocatalysts. *Materials Research Bulletin*, 2020. 131: p. 110965.
- [18] Uthirakumar, P., et al., Efficient, recyclable, and affordable daylight induced  $\text{Cu}/\text{Cu}_2\text{O}/\text{CuI}$  photocatalyst via an inexpensive iodine sublimation process. *Applied Surface Science*, 2021. 537: p. 147007.
- [19] Fang, K., et al., Synthesis of novel magnetically separable  $\text{Fe}_3\text{O}_4/\text{Bi}_2\text{O}_3/\text{Bi}_2\text{O}_3/\text{Bi}_2\text{O}_3$  photocatalyst with boosted visible-light photocatalytic activity. *Materials Research Bulletin*, 2020. 129: p. 110888.
- [20] Fu, Y., et al., High photocatalytic activity of magnetically separable manganese ferrite-graphene heteroarchitectures. *Industrial & engineering chemistry research*, 2012. 51(2): p. 725-731.
- [21] Rahman, A., et al., Cd-Gd-doped nickel spinel ferrite nanoparticles and their nanocomposites with reduced graphene oxide for catalysis and antibacterial activity studies. *Ceramics International*, 2021. 47(7): p. 9513-9521.

- [22] Kambale, R., et al., Effect of cobalt substitution on structural, magnetic and electric properties of nickel ferrite. *Journal of Alloys and Compounds*, 2009. 478(1-2): p. 599- 603.
- [23] Zhang, J., et al., Nanoscale characterization and magnetic reversal mechanism investigation of electrospun NiFe<sub>2</sub>O<sub>4</sub> multi-particle-chain nanofibres. *Nanoscale*, 2012. 4(8): p. 2754-2759.
- [24] Dutta, V., et al., Review on augmentation in photocatalytic activity of CoFe<sub>2</sub>O<sub>4</sub> via heterojunction formation for photocatalysis of organic pollutants in water. *Journal of Saudi Chemical Society*, 2019. 23(8): p. 1119-1136.
- [25] Naik, M.M., et al., Green synthesis of zinc doped cobalt ferrite nanoparticles: Structural, optical, photocatalytic and antibacterial studies. *Nano-Structures & Nano-Objects*, 2019. 19: p. 100322.
- [26] Chandel, N., et al., Magnetically separable ZnO/ZnFe<sub>2</sub>O<sub>4</sub> and ZnO/CoFe<sub>2</sub>O<sub>4</sub> photocatalysts supported onto nitrogen doped graphene for photocatalytic degradation of toxic dyes. *Arabian Journal of Chemistry*, 2020. 13(2): p. 4324-4340.
- [27] Singh, P., et al., Systematic review on applicability of magnetic iron oxides-integrated photocatalysts for degradation of organic pollutants in water. *Materials Today Chemistry*, 2019. 14: p. 100186.
- [28] Singh, P., et al., Photocatalytic performance and quick recovery of BiOI/Fe<sub>3</sub>O<sub>4</sub>@ graphene oxide ternary photocatalyst for photodegradation of 2, 4-dinitrophenol under visible light. *Materials Today Chemistry*, 2019. 12: p. 85-95.
- [29] Chakrabarty, S., A. Dutta, and M. Pal, Enhanced magnetic properties of doped cobalt ferrite nanoparticles by virtue of cation distribution. *Journal of Alloys and Compounds*, 2015. 625: p. 216-223.
- [30] Mallapur, M., et al., Structural and electrical properties of nanocrystalline cobalt substituted nickel zinc ferrite. *Journal of alloys and compounds*, 2009. 479(1-2): p. 797-802.
- [31] Debnath, S., A. Das, and R. Das, Effect of cobalt doping on structural parameters, cation distribution and magnetic properties of nickel ferrite nanocrystals. *Ceramics International*, 2021. 47(12): p. 16467-16482.
- [32] Khalid, N., et al., Cu-doped TiO<sub>2</sub> nanoparticles/graphene composites for efficient visible-light photocatalysis. *Ceramics International*, 2013. 39(6): p. 7107-7113.
- [33] Rafique, M., et al., Facile hydrothermal synthesis of highly efficient and visible light-driven Ni-doped V<sub>2</sub>O<sub>5</sub> photocatalyst for degradation of Rhodamine B dye. *Journal of Materials Science: Materials in Electronics*, 2020. 31: p. 12913-12925.
- [34] Rafique, M., et al., Plant-mediated green synthesis of zinc oxide nanoparticles from *Syzygium Cumini* for seed germination and wastewater purification. *International Journal of Environmental Analytical Chemistry*, 2022. 102(1): p. 23-38.
- [35] Tahir, M.B., et al., Nanostructured-based WO<sub>3</sub> photocatalysts: recent development, activity enhancement, perspectives and applications for wastewater treatment. *International Journal of Environmental Science and Technology*, 2017. 14: p. 2519-2542.
- [36] Shakil, M., et al., Enhanced structural, optical, and photocatalytic activities of Cd-Co doped Zn ferrites for degrading methyl orange dye under irradiation by visible light. *Journal of Physics and Chemistry of Solids*, 2022. 161: p. 110419.
- [37] Mohammadzadeh Kakhki, R., et al., Visible light photocatalytic degradation of textile waste water by Co doped NiFe<sub>2</sub>O<sub>4</sub> nanocomposite. *Journal of Materials Science: Materials in Electronics*, 2017. 28: p. 4095-4101.
- [38] Cai-Yun, L., Y. Zheng-Feng, and B. Paul, Facile synthesis of spinel CoFe<sub>2</sub>O<sub>4</sub> nanoparticle and its application as magnetic recoverable photocatalyst for degradation of metronidazole and some selected organic dyes. *Journal of nanoscience and nanotechnology*, 2020. 20(2): p. 1209-1214.
- [39] Jadhav, S.A., et al., Magnetically retrievable nanoscale nickel ferrites: an active photocatalyst for toxic dye removal applications. *Ceramics International*, 2021. 47(20): p. 28623- 28633.
- [40] Chahar, D., et al., Photocatalytic activity of cobalt substituted zinc ferrite for the degradation of methylene blue dye under visible light irradiation. *Journal of Alloys and Compounds*, 2021. 851: p. 156878.
- [41] Kant, R. and A.K. Mann, A review of doped magnesium ferrite nanoparticles: introduction, synthesis techniques and applications. *IJSRSET*, 2018. 4(7).
- [42] Gupta, N., et al., Current development in synthesis and characterization of nickel ferrite nanoparticle. *Materials Today: Proceedings*, 2017. 4(2): p. 342-349.
- [43] Yadav, R.S., et al., Sonochemical synthesis of Gd<sup>3+</sup> doped CoFe<sub>2</sub>O<sub>4</sub> spinel ferrite nanoparticles and its physical properties. *Ultrasonics sonochemistry*, 2018. 40: p. 773-783.
- [44] Hai, A., et al., Cobalt and nickel ferrites based capacitive deionization electrode materials for water desalination applications. *Electrochimica Acta*, 2020. 363: p. 137083.
- [45] Chakradhary, V.K., A. Ansari, and M.J. Akhtar, Design, synthesis, and testing of high coercivity cobalt doped nickel ferrite nanoparticles for magnetic applications. *Journal of Magnetism and Magnetic Materials*, 2019. 469: p. 674-680.
- [46] Sowjanya, P., et al., Synthesis and analysis of low field high magnetostrictive Ni-Co ferrite for magneto-electric energy harvesting applications. *Materials Science and Engineering: B*, 2022. 279: p. 115674.
- [47] Torkian, S., A. Ghasemi, and R.S. Razavi, Cation distribution and magnetic analysis of wideband microwave absorptive Co<sub>x</sub>Ni<sub>1-x</sub>Fe<sub>2</sub>O<sub>4</sub> ferrites. *Ceramics International*, 2017. 43(9): p. 6987-6995.
- [48] Ati, A.A., Fast synthesis, structural, morphology with enhanced magnetic properties of cobalt doped nickel ferrite nanoscale. *Journal of Materials Science: Materials in Electronics*, 2018. 29: p. 12010-12021.
- [49] Pubby, K., K.V. Babu, and S.B. Narang, Magnetic, elastic, dielectric, microwave absorption and optical characterization of cobalt-substituted nickel spinel ferrites. *Materials Science and Engineering: B*, 2020. 255: p. 114513.